# Influence of predefined angle of attack on piezoelectric energy harvesting from transverse galloping of different bluff bodies

**Mingjie Zhang[1], Haiyan Yu[2], Daniil Yurchenko[3], Junlei Wang[4,*], Fuyou Xu[5,**], Cristoforo Demartino[6, 7]**

*1. Department of Structural Engineering, Norwegian University of Science and Technology, Trondheim 7491, Norway.*

*2. School of Civil and Environmental Engineering, Harbin Institute of Technology, Shenzhen 518055, China.*

*3. Institute of Mechanical, Process & Energy Engineering, Heriot-Watt University, Edinburgh EH14 4AS, UK.*

*4. School of Mechanical and Power Engineering, Zhengzhou University, Zhengzhou 450000, China.*

*5. School of Civil Engineering, Dalian University of Technology, Dalian, 116024, China*

*6. Zhejiang University - University of Illinois at Urbana Champaign Institute, Zhejiang University, Haining 314400, China.*

*7. Department of Civil and Environmental Engineering, University of Illinois at Urbana-Champaign, Urbana, IL 61801, USA.*

*Corresponding author: Junlei Wang, Email address: jlwang@zzu.edu.cn

**Corresponding author: Fuyou Xu, Email address: fuyouxu@hotmail.com

**Abstract:** The development of smart Internet-of-Things (IoT) solutions requires sensor nodes to be placed at different locations of monitored structures. Wireless solutions are quite attractive because of their simplicity although requiring for local energy supply. In this context, this study investigates the influences of the predefined angle of attack on the piezoelectric energy harvesting based on transverse galloping of different bluff bodies. The investigation is based on a lumped electro-aero-mechanical model with linear electrical and mechanical properties and nonlinear aerodynamic forces evaluated using the quasi-steady theory. The performances of energy harvesters with six different bluff bodies are analyzed at various predefined angles of attack: four rectangular cross-sections with different width-to-height ratios (i.e., $b/d$), one trapezium section, and one equal angle section. The main purpose is to understand the sensitivity of various bluff body-based energy harvesters on the predefined angle of attack, and further suggest a bluff body-based energy harvester that is robust to the predefined angle of attack. The results show that the response is quite dependent on the characteristic of the electro-mechanical system and the bluff body cross-section and angle of attack. In all cases, the load resistance should be tuned to maximize energy production. The largest vibration amplitude (i.e., largest power output) is predicted for the rectangular bluff body with $b/d$ = 1.0 at a 0° angle of attack. However, its performances are quite dependent on the angle of attack, resulting in a zero-power output for an angle of attack exceeding 4°. A rectangular bluff body with $b/d$ within 1.62 to 2.5 exhibits a reduced energy production compared with $b/d$ = 1.0 at a 0° angle of attack but better robustness varying the angle of attack. Finally, the trapezium and the angle bluff bodies are not suitable for energy harvesting due to their very high onset velocities within the considered range of angles of attack.

**Keywords:** Flow energy harvesting; transverse galloping; bluff body configuration; angle of attack

## 1. Introduction

As a typical type of flow-induced vibration, transverse galloping may occur for a flexible structure as the oncoming flow velocity increases over an onset value. This dynamical instability has been experienced by a great variety of engineering structures with different cross-sections, e.g., rectangular sections [1-3], D-sections [4], triangular sections [5], and modified circular sections (e.g., a circular section with ice accretions or a circular section with splitter plate) [6]. Transverse galloping is often considered an undesirable vibration since it may reduce the structural service life or lead to fatigue failure [7, 8]. Beneficial consequences of transverse galloping include converting mechanical vibrations into electric power and hence harvesting energy from flowing wind or water [9-15].

The study of transverse galloping can be tracked back to Den Hartog [16], who proposed the well-known instability criterion based on the quasi-steady theory. The group of Parkinson [2, 17] tested the transverse galloping of several different cross-sections and proposed a nonlinear quasi-steady model to simulate the aeroelastic forces on the vibrating structure. The transverse galloping of structures with different cross-sections was investigated in the following decades, with extensive efforts paid to simulate the structural vibrations due to transverse galloping [7, 10, 18], and/or mitigate the deleterious vibrations [19, 20]. It is now well-known that the quasi-steady model can accurately simulate the transverse galloping of a structure with a relatively large value of the mass-damping parameter. However, for a structure that has a very low mass-damping parameter, the onset velocity for galloping is low and the quasi-steady model becomes inapplicable [8, 21]. To ensure the reliability of flexible structures immersed in air/water flow, both aerodynamic countermeasures [22, 23] and mechanical countermeasures [19, 20] have been proposed to mitigate the undesired vibrations due to transverse galloping.

Barrero-Gil et al. [24] demonstrated the feasibility of harvesting wind energy based on transverse galloping using a lumped-parameter numerical system with the quasi-steady aerodynamic model. They [25, 26] further attempted to investigate the effectiveness of galloping-based energy harvesters with various bluff body configurations and optimize the mechanical and electrical parameters to enhance energy harvesting. Abdelkefi and co-authors [9, 27-31] presented a series of investigations focusing on the effects on energy harvesting of various aspects, including the tip body shape, the representation of aerodynamic force, and the wind yaw angle, etc. Yang et al. [32] presented wind tunnel experiments to study the performances of galloping-based energy harvesters with the square, rectangular, and triangular cross-sections of the bluff bodies. A comparison of these energy harvesters showed that the harvester with a square cylinder has the best performance. Zhao et al. [33] studied the effect of modeling methods of the electromechanical models and presented a parametric study for

the transverse galloping-based energy harvester. Hémon et al. [34] and Andrianne et al. [35] carried out wind tunnel tests to investigate wind energy harvesting based on flow-induced vibrations of rectangular cylinders. Zhang et al. [36] studied the influences of structural damping ratio, mass ratio, and width-to-height ratio on the energy harnessing from flow-induced vibration of rectangular bluff bodies. They focused on energy harvesters with relatively low mass ratios, which exhibit interfered vortex-induced vibration and galloping.

Although a lot of investigations have been conducted to investigate the energy harvesting from transverse galloping, most existing studies predefined a 0° angle of attack of the bluff body relative to the oncoming flow. The influences of the variable predefined angle of attack on the effectiveness of the galloping-based energy harvester have rarely been studied. For a practical energy harvester operating in the natural wind, the angle of attack may vary with the wind direction, and it is hence important to study the performance of the energy harvester within the possible range of angles of attack. An energy harvester can be considered as lacking robustness if its performance is very sensitive to the predefined angle of attack. For a square cylinder, the dependency of flow-induced vibrations on the predefined angle of attack has been demonstrated in [37, 38]. More recently, it is shown that the performance of a square cylinder-based energy harvester is also dependent on the predefined angle of attack [39, 40]. However, a systematic study on the effects of the predefined angle of attack on energy harvesting from transverse galloping of different bluff bodies remains unavailable. The predefined angle of attack is here and in the following defined as the initial angle of attack, i.e., the angle between the mean flow direction and the $x$ local axis (see Figure 1(b)). Generally, the angle of attack can change for two reasons: (i) when the oncoming mean wind is changing direction (e.g., atmospheric wind), and (ii) when the cross-section is rotated. The first case is typical of harvesters installed in an atmospheric boundary layer while the second is typical of harvesters with active control of the cross-section.

This paper investigates numerically the effects of the predefined angle of attack on the transverse galloping-based energy harvesting using different cross-sections as the tip body. The main purpose is to understand the sensitivity of various bluff body-based energy harvesters on the predefined angle of attack, and further suggest a bluff body-based energy harvester that is robust to the predefined angle of attack. Following the authors' previous studies, the electro-mechanical system is described by a linear lumped-parameter model while the nonlinear aerodynamic force is described by the quasi-steady model. Bluff bodies with six different cross-sections are considered, i.e., four rectangular sections of different side ratios, a trapezium section, and an angle section. The experimental aerodynamic coefficients from Norberg et al. [41], Feero et al. [42], Luo et al. [43], and Slater [44] are used as input parameters of the aerodynamic force model. The lumped-parameter model for a galloping-based piezoelectric energy harvester is introduced in Section 2. The effects of predefined angle

of attack and tip body cross-section on the onset velocity for galloping are studied in subsection 3.1. The effects of predefined angle of attack on the displacements and power outputs of galloping-based harvesters with various bluff bodies are discussed in subsection 3.2.The main conclusions are summarized in Section 4.

## 2. Modeling and validation

### 2.1. Aero-electro-mechanical modeling

Figure 1 presents a schematic illustration of the considered energy harvester and the bluff body configurations, where $b$ is the width and $d$ is the height of the bluff body. As schematically shown in Figure 1(a), the transverse galloping-based energy harvester includes a bluff body, a cantilever beam, and a piezoelectric transducer. Figure 1(b) shows the definition of the predefined angle of attack $\alpha_0$, which is the angle between the oncoming flow direction and the $x$ local axis of the bluff body in its static configuration. Following the authors' previous papers [39, 45], the aero-electro-mechanical system can be simplified as a lumped-parameter model as:

$$m[\ddot{y}(t) + 2\omega_0\xi_0\dot{y}(t) + \omega_0^2 y(t)] + \theta V(t) = F_y(t) \tag{1a}$$

$$\frac{V(t)}{R} + C_p\dot{V}(t) - \theta\dot{y}(t) = 0 \tag{1b}$$

where $m$ is the equivalent mass of the energy harvester per unit length, $y$ denotes the transverse displacement of the bluff body, the overdot means the time derivative, $\omega_0$ denotes the natural frequency, $\xi_0$ denotes the mechanical damping ratio, $F_y$ represents the aeroelastic force acting on the bluff body per unit length, $V$ is the generated voltage, $C_p$ denotes the capacitance of the piezoelectric layer, $R$ is the electrical load resistance, and $\theta$ represents the electromechanical coupling coefficient. It is noted that the following assumptions are involved in Eq. (1): (i) the electrical circuit is well-established so that the electrical nonlinearity is insignificant; (ii) the mechanical system is well-established so that the mechanical nonlinearity is insignificant; (iii) two-dimensional flow is assumed along the cylinder while the three-dimensional flow around two ends of the cylinder is not considered; and (iv) the cylinder itself is assumed as a rigid body and hence only the rigid-body motion of the cylinder is considered.

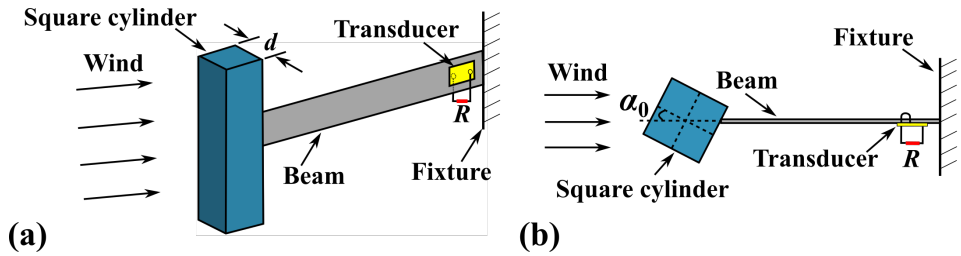

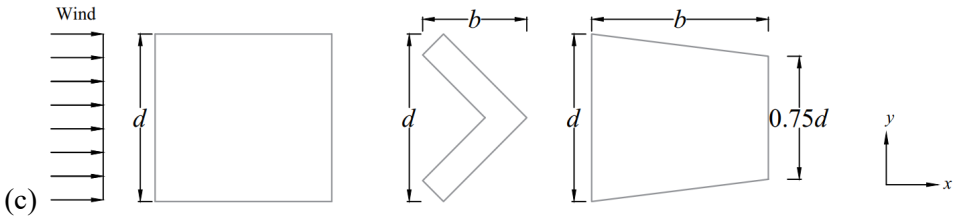


**Figure 1.** Galloping-based energy harvester: (a) schematic of energy harvester, (b) definition of predefined angle of attack, and (c) cross-sections of bluff bodies.

The aerodynamic force for uniform oncoming flow can be approximated using the quasi-steady model as:

$$F_y = 0.5\rho U^2 d C_{Fy} = 0.5\rho U^2 d \sum_{j=1}^{J} A_j \left(\alpha_0 + \frac{\dot{y}}{U}\right)^j \tag{2}$$

where $\rho$ is the fluid density, $U$ is the oncoming flow velocity, $d$ is the dimension of the bluff body perpendicular to the cross-flow as shown in Figure 1(c), $C_{Fy}$ represents the aerodynamic lift force coefficient (which is a nonlinear function of the angle of attack), and $A_j$ ($j = 1 \sim J$) are aerodynamic damping coefficients which can be calculated based on the experimental $C_{Fy}(\alpha)$ curve using the least square fitting. $\dot{y}/U$ is the variation of the angle of attack due to the structural motion and $\alpha_0 + \dot{y}/U$ is the relative angle of attack. In fact, the quasi-steady theory assumes that the aerodynamic forces are nonlinear depending on the structural velocity which is modifying the angle of attack. Equation (2) is not considering the effect of vortex shedding because the shedding frequency is much higher than the structural natural frequency under unstable conditions.

For a cross-section that is symmetric about the chord line, an accurate approximation can be achieved by including only odd-order terms ($j = \{1, 3, 5, \ldots\}$) in equation (2) [3, 10]. The key assumption involved in the quasi-steady theory is that that the aerodynamic force on a vibrating body can be approximated by the force on a stationary one, as long as the configuration of the latter is identical to the instantaneous configuration of the former. This assumption is acceptable only if the time scale for the incident flow to pass through the cylinder and arrive sufficiently far downstream is considerably lower than that of the cylinder vibration [3]. As a result, the quasi-steady theory is capable of accurately simulating the galloping of a square cylinder with relatively high onset reduced velocities $U_r = U/\omega_0 d$ (in other words, cases with high values of the mass-damping parameters), while its accuracy decreases with decreasing mass-damping parameter [46, 47].

By substituting quasi-steady aerodynamic force into equation (1) and introducing some dimensionless variables $\tau = \omega_0 t$, $Y = y/d$, and $I = \theta V/m\omega_0^2 d$, equation (1) can be expressed as:

$$Y'' + 2\xi_0 Y' + Y + I = \frac{U_r^2}{2m^*} \sum_{j=1}^{J} A_j \left(\alpha_0 + \frac{Y'}{U_r}\right)^j \tag{3a}$$

$$I + C_p R \omega_0 I' = 2\xi_E Y' \tag{3b}$$

where the prime indicates the derivative with respect to the dimensionless time $\tau$, $m^* = m/\rho d^2$ quantifies the mass ratio between the harvester and the displaced fluid, $\xi_E = \theta^2 R/2m\omega_0$ represents the dimensionless damping coefficient due to the electrical coupling effect. Validations of the lumped-parameter model described by equations (1) and (3) can be found in the authors' previous papers [39, 45]. In [39], the effect of predefined angle of attack is investigated for a square cylinder-based energy harvester. This paper systematically studies the effects of predefined angle of attack on the transverse galloping-based energy harvesting using different bluff bodies.

**2.2. Linear stability of the system: onset galloping velocity**

The onset galloping velocity for the coupled system described in equation (3) is analyzed in this subsection. First, the following state variables are introduced based on Equation (3):

$$\mathbf{X} = \begin{bmatrix} X_1 \\ X_2 \\ X_3 \end{bmatrix} = \begin{bmatrix} Y \\ Y' \\ I \end{bmatrix} \tag{4}$$

For a specific predefined angle of attack $\alpha_0$, equation (3) can be linearized (around the original static configuration of the bluff body in its static) as:

$$X_1' = X_2 \tag{5a}$$

$$X_2' = -X_1 - (2\xi_0 - \frac{U_r}{2m^*}S)X_2 - X_3 \tag{5b}$$

$$X_3' = \frac{2\xi_E X_2}{C_p R\omega_0} - \frac{X_3}{C_p R\omega_0} \tag{5c}$$

where $S$ is the linearized version of the aerodynamic coefficient at $\alpha_0$, i.e., $S = \left.\frac{d\sum_{j=1}^{J} A_j(\alpha)^j}{d\alpha}\right|_{\alpha=\alpha_0}$.

Equation (5) can be expressed in a matrix form as:

$$\mathbf{X}' = \mathbf{G}\mathbf{X} \tag{6a}$$

$$\mathbf{G} = \begin{bmatrix} 0 & 1 & 0 \\ -1 & -(2\xi_0 - \frac{U_r}{2m^*}S) & -1 \\ 0 & \frac{2\xi_E}{C_p R\omega_0} & -\frac{1}{C_p R\omega_0} \end{bmatrix} \tag{6b}$$

The matrix **G** includes all parameters that affect the stability of the coupled system. Therefore, this matrix can be used to investigate the influences of the angle of attack and the corner shape on the onset velocity of galloping.

The characteristic equation of matrix **G** is:

$$\det[\mathbf{G}-\boldsymbol{\lambda}\mathbf{I}]=\boldsymbol{\lambda}^3+\boldsymbol{\lambda}^2\left(2\xi_0+\frac{1}{C_pR\omega_0}-\frac{U_rS}{2m^*}\right)+\boldsymbol{\lambda}\left(1+\frac{2\xi_0}{C_pR\omega_0}+\frac{2\xi_E}{C_pR\omega_0}-\frac{U_rS}{2m^*C_pR\omega_0}\right)+\frac{1}{C_pR\omega_0}=\mathbf{0} \tag{7}$$

The three eigenvalues of the coupled system can be calculated through a complex eigenvalue analysis of matrix **G**. Because of the electromechanical coupling effect, the coupled system has a real eigenvalue which is always negative. In addition, the coupled system has a pair of complex eigenvalues that determines its stability. The two eigenvalues are a pair of complex conjugates, and the onset galloping velocity is achieved when the real part of the two eigenvalues becomes zero. The onset galloping velocity for a pure single-degree-of-freedom aeroelastic system (that is, a system without the piezoelectric coupling effect) [3, 10] is $U_r = 4m^*\xi_0/S$.

### 2.3. Input data of the electro-aero-mechanical system

Bluff bodies with six different cross-sections are considered in the following analyses, i.e., rectangular sections of side ratio $b/d$ = 1.0, 1.62, 2.0, and 2.5, a trapezium section, and an angle section, as illustrated in Figure 1(c), in which $b$ is the dimension of the bluff body parallel to the cross-flow. The considered rectangular cylinders have been largely investigated for energy harvesting at a 0° angle of attack. Rectangular bluff bodies with width-to-height ratios out of the aforementioned range are not considered either because they have very high onset galloping velocities or they are always stable [41, 42]. The other two cross-sections, i.e., the trapezium section and the angle section, are also known to be prone to galloping instability [43, 44]. Aerodynamic coefficients of the considered cross-sections are presented in Figure 3. The aerodynamic coefficients of a $b/d$ = 3.0 rectangular section are also presented while this section is not analyzed in the following parts since it is stable from galloping due to the negative slope of the $C_{Fy}(\alpha)$ curve (and hence negative $A_1$ value). Aerodynamic coefficients are asymmetric about $\alpha$ = 0° since the considered cross-sections are symmetric about their chord lines. The experimentally obtained coefficients are fitted by using 17$^{th}$-order polynomials (only with odd-order terms) with $A_i$ listed in Table 1. It is noted that, for the rectangular sections with $b/d$ = 1.0 and 3.0, the aerodynamic coefficients measured by Norberg et al. [41] and Ferro et al. [42] agree very well. Hence, the data of Norberg et al. [41] and Ferro et al. [42] can be utilized together to compare the performances of energy harvesters with rectangular bluff bodies of different side ratios. It should be stated that the aerodynamic coefficients may be dependent on several parameters, e.g., the turbulent intensity and the Reynolds number. However, the effects of these parameters are not considered in the present study.

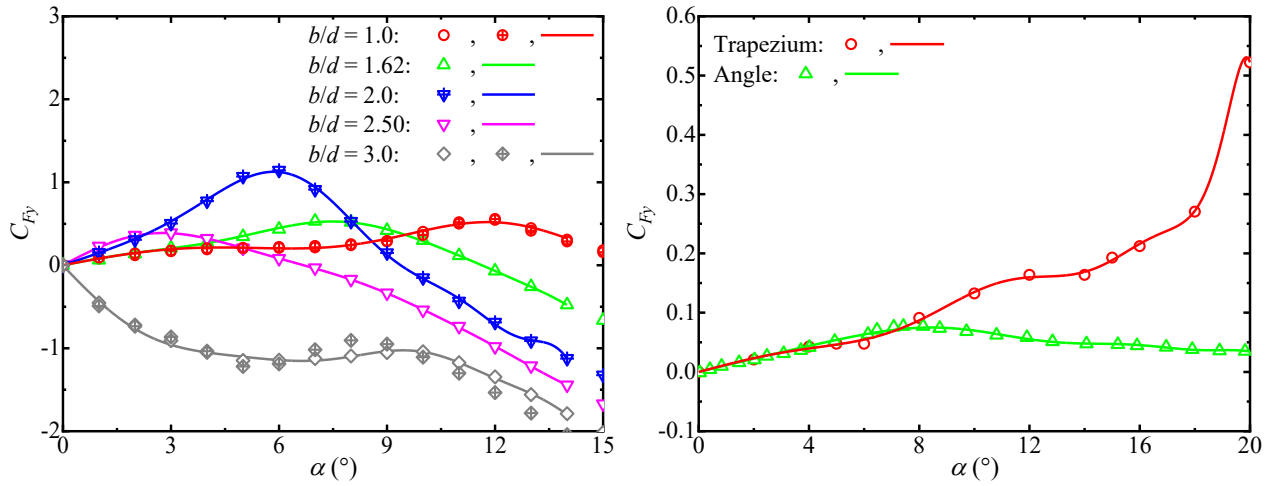


**Figure 3.** Experimental and fitted aerodynamic coefficients of various cross-sections: (a) rectangular sections of different side ratios, open markers from [41], and crossed markers from [42]; (b) trapezium section [43] and angle section [44].

**Table 1.** Polynomial representations of the aerodynamics coefficients

| Cylinder | $A_1$ | $A_3$ | $A_5$ | $A_7$ | $A_9$ | $A_{11}$ | $A_{13}$ | $A_{15}$ | $A_{17}$ |
|---|---|---|---|---|---|---|---|---|---|
| Rec 1.0 [42] | 4.68 | −3.99e2 | 1.19e4 | 3.85e5 | −2.61e7 | 5.34e8 | −5.28e9 | 2.58e10 | −5.00e10 |
| Rec 1.62 [41] | 4.82 | −6.22e2 | 1.29e5 | −1.09e7 | 4.70e8 | −1.16e10 | 1.66e11 | −1.30e12 | 4.28e12 |
| Rec 2.0 [42] | 8.46 | −1.72e2 | 3.68e5 | −6.09e7 | 4.04e9 | −1.40e11 | 2.66e12 | −2.67e13 | 1.09e14 |
| Rec 2.5 [42] | 13.0 | −2.61e3 | 2.36e5 | −1.27e7 | 4.14e8 | −8.21e9 | 9.72e10 | −6.30e11 | 1.71e12 |
| Trapezium[43] | 0.71 | −3.81e1 | 1.48e3 | 9.62e4 | −6.82e6 | 1.62e8 | −1.88e9 | 1.07e10 | −2.39e10 |
| Angle [44] | 0.65 | −6.91 | 8.20e2 | −7.44e4 | 2.43e6 | −3.92e7 | 3.39e8 | −1.51e9 | 2.72e9 |

## 3. Results and discussions

The influences of the predefined angle of attack are investigated for various energy harvesters with different tip bluff bodies. It is assumed that all cylinders have a unit length and the same $d$ = 0.015 m. The mechanical and electrical parameters are $m^* = 1564.4$, $\xi_0$ = 0.13%, $\theta$ = 1.55 mN/V, and $C_p$ = 120 nF, as considered in [27]. The natural frequency of the cylinder without aerodynamic and piezoelectric coupling is $f_0$ =10 Hz. As indicated by the eigenvalue analysis, the natural frequency of the coupled system can be slightly affected by the presence of the piezoelectric terms. However, the natural frequency remains close to 10 Hz for the considered cases. It should be stated that this paper considers a system with linear electrical and mechanical behaviors that are governed by equation (1). The main results for systems with nonlinear electrical and mechanical behaviors should be qualitatively similar.

### 3.1. Onset galloping velocity

The effects of the angle of attack on the onset galloping velocity of energy harvesters with different bluff bodies are analyzed in this subsection. Figure 4 presents the variations of the onset galloping velocities versus the electrical load resistance for energy harvesters with different bluff bodies and angles of attack. For each

bluff body, the range of predefined angles of attack $\alpha_0 = 0° \sim 6°$ are considered since the aerodynamic lift coefficients are available in a limited range of angles of attack. It is noted that the range of angles of attack for a practical energy harvester may depend on several factors including the wind environment and the location of the cylinder. The square cross-section ($b/d = 1.0$) is always stable at $\alpha_0 = 5°$ and 6°, the rectangular section of $b/d = 2.0$ is stable at $\alpha_0 = 6°$, while the rectangular section of $b/d = 2.5$ is stable at $\alpha_0 = 3°$, 4°, 5°, and 6° (this is expected since the slope S becomes negative). Other cross-sections are unstable from galloping within the considered range of angles of attack. It is noted that the onset galloping velocities of all bluff bodies are affected by the angle of attack. The onset velocities for the $b/d = 1.0$ and 2.5 rectangular cylinders increase significantly with increasing the angle of attack. For other bluff bodies, the onset velocities vary non-monotonically with increasing the angle of attack, and the effects of the angle of attack on the onset velocities are less significant.

For a load resistance of $R = 10^6$ Ω, the onset galloping velocities for energy harvesters with different bluff bodies at various angles of attack are listed in Table 2. At the angle of attack $\alpha_0 = 0°$, the onset galloping velocities of the rectangular cylinders can be decreased by increasing the side ratio, and the lowest onset velocity is achieved by the $b/d = 2.5$ rectangular cylinder. On the other hand, the $b/d = 1.62$ and 2.0 rectangular cylinders should be recommended if the energy harvester is expected to have low onset velocities within a relatively wide range of angles of attack. Finally, the trapezium section and the angle section are not suitable for energy harvesting due to their very high onset velocities within the considered range of angles of attack.

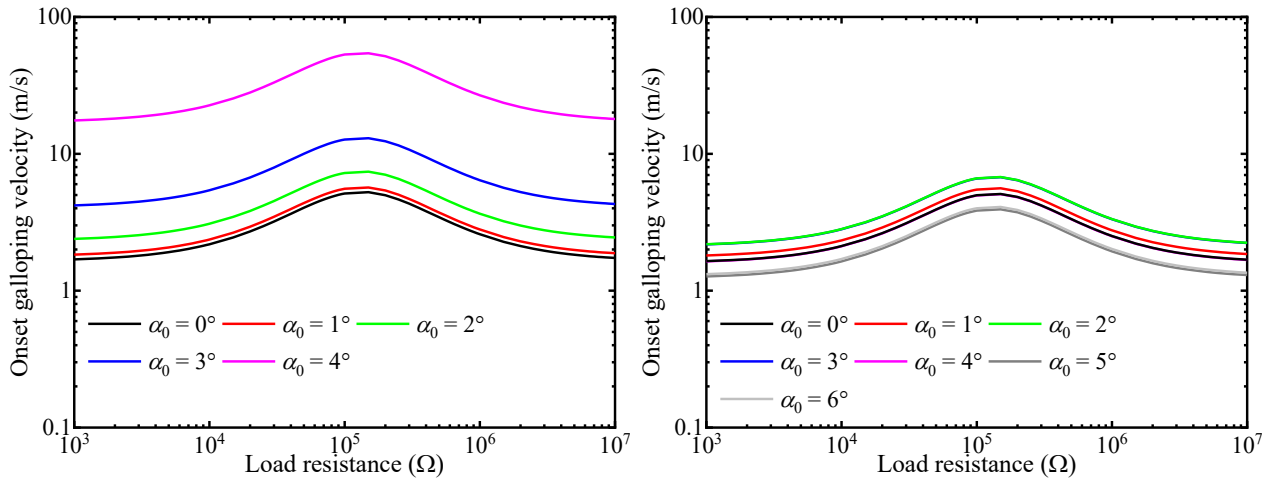


(a) (b)

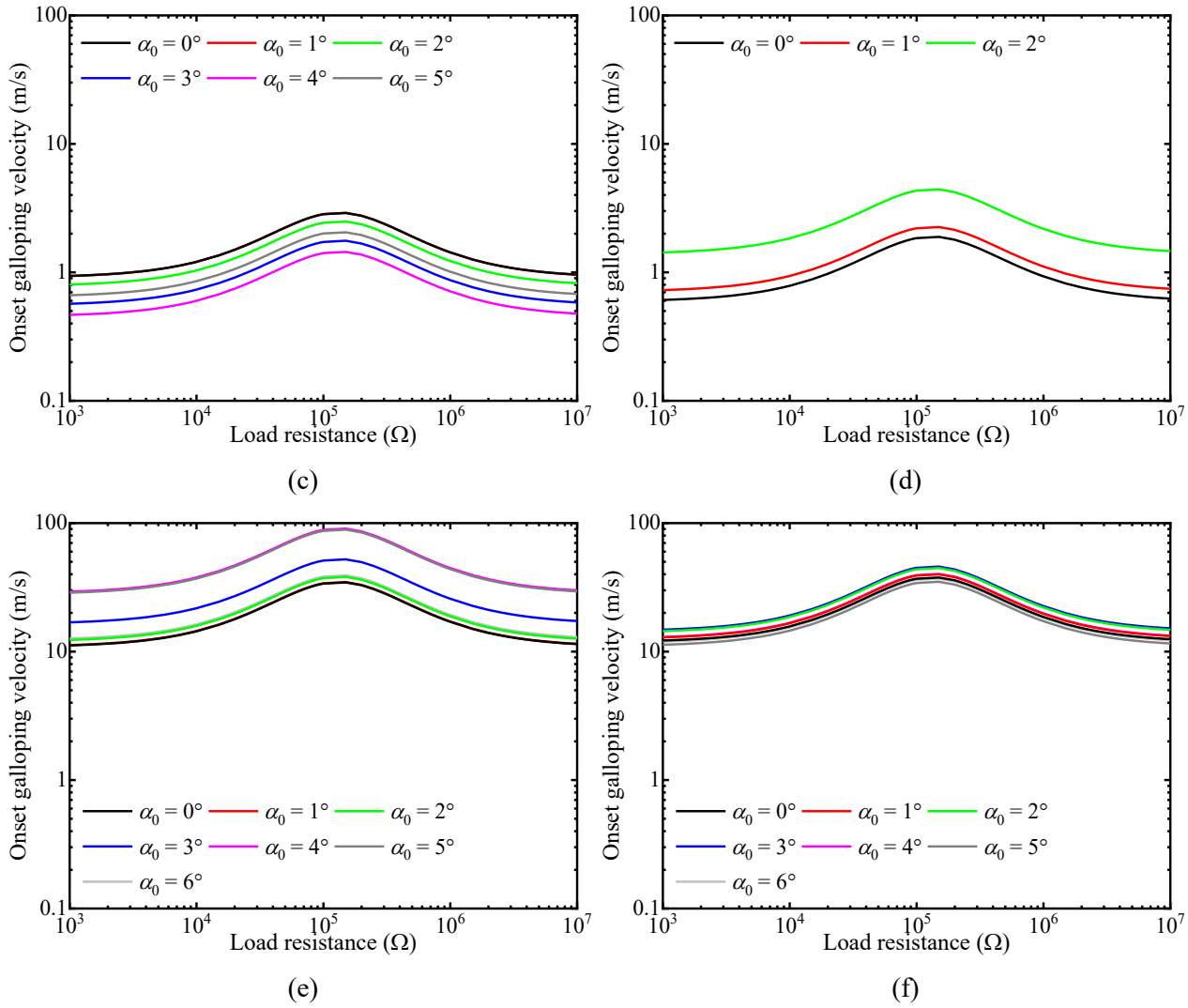


**Figure 4.** Variations of onset galloping velocities versus electrical load resistance for energy harvesters with various bluff bodies: (a) rectangular section of $b/d$ = 1.0; (b) rectangular section of $b/d$ = 1.62; (c) rectangular section of $b/d$ = 2.0; (d) rectangular section of $b/d$ = 2.5; (e) trapezium section; (f) angle section. (load resistance $R = 10^6$ Ω and natural frequency $f_0$ =10 Hz).

**Table 2.** Onset galloping velocities (m/s) for energy harvesters with load resistance $R = 10^6$ Ω and natural frequency $f_0$ =10 Hz.

| $\alpha_0$ (°) | Rec 1.0 | Rec 1.62 | Rec 2.0 | Rec 2.5 | Trapezium | Angle |
|---|---|---|---|---|---|---|
| 0 | 2.58 | 2.51 | 1.43 | 0.93 | 17.04 | 18.61 |
| 1 | 2.80 | 2.81 | 1.43 | 1.13 | 17.15 | 18.78 |
| 2 | 3.65 | 3.59 | 1.23 | 2.39 | 18.80 | 19.20 |
| 3 | 6.41 | 3.80 | 0.87 | stable | 25.77 | 19.69 |
| 4 | 26.77 | 2.87 | 0.71 | stable | 44.70 | 20.25 |
| 5 | stable | 2.20 | 1.01 | stable | 43.84 | 21.47 |
| 6 | stable | 2.34 | stable | stable | 19.32 | 24.96 |

### 3.2. Displacements and power

The displacement and voltage output of the nonlinear electro-aero-mechanical system after the onset galloping velocity can be obtained by solving equation (3) in the time domain. Equations (3a) and (3b) are

solved by numerical integration by using the Newmark-β method with average constant acceleration ($\gamma = 0.5$ and $\beta = 0.25$). The considered bluff bodies are the rectangular sections of $b/d$ = 1.0, 1.62, 2.0, and 2.5, while bluff bodies with trapezium and angle sections are not analyzed in this section due to their very high onset velocities within the considered range of angles of attack. For a specific combination of bluff body configuration and angle of attack, the displacement and voltage outputs are simulated within an oncoming flow velocity range of 0 to 15 m/s. The corresponding reduced velocity range is $U_r = U/(\omega_0 d) = 0 \sim 15.9$. The simulations are conducted by increasing the flow velocity with a 0.2 m/s step. The initial displacement for a specific flow velocity is adopted as the formerly analyzed flow velocity. It is noted that the steady-state displacements and power output of the energy harvester may be different if the simulation is performed by increasing or decreasing the oncoming flow velocity. For example, for a system that exhibits a saddle-node bifurcation and a subcritical Hopf bifurcation, the steady-state displacements and power outputs are dependent on the initial displacement for flow velocities between the saddle-node and subcritical Hopf bifurcations. Details of the bifurcation behaviors can be found in [48] and will be discussed later.

The variations of the dimensionless transverse displacements versus the load resistance for energy harvesters with the different rectangular bluff bodies and angles of attack are presented in Figures 5(a, c, e), Figures 6(a, c, e), Figures 7(a, c, e), and Figures 8(a, c, e), respectively. Three flow velocities are considered, i.e., $U$ = 4, 8, and 14 m/s. It is again noted that the rectangular section of $b/d$ = 1.0 is stable from galloping at $\alpha_0$ = 5° and 6°, the rectangular section of $b/d$ = 2.0 is stable at $\alpha_0$ = 6°, the rectangular section of $b/d$ = 2.5 is stable at $\alpha_0$ = 3°, 4°, 5°, and 6°, while the rectangular section of $b/d$ = 1.62 is unstable from galloping within the considered range of angles of attack. It follows from these figures that the displacements initially reduces and then enlarges with increasing the load resistance for all rectangular cylinders. The minimum displacements are achieved at a load resistance close to $R = 10^5$ Ω. This observation is due to the maximum damping induced by the electrical coupling effect around this load resistance range. For some cases with specific parameter combinations in Figures 5(a) and 6(a), the displacements are zero since the onset galloping velocities for these cases are higher than 4 m/s. The transverse displacements of all bluff bodies are remarkably affected by the angle of attack. For each bluff body, the vibration amplitude at a specific flow velocity and load resistance generally decreases with increasing the angle of attack with some exceptions where the vibration amplitude exhibits a sudden jump.

Figures 5(b, d, f), Figures 6(b, d, f), Figures 7(b, d, f), and Figures 8(b, d, f) show the variations of the power outputs versus the load resistance for energy harvesters with rectangular cylinders of various side ratios. The power is calculated as $V^2/2R$. For each bluff body, the power output at a specific flow velocity and load

resistance generally decreases with increasing the angle of attack with some exceptions where the vibration amplitude exhibits a sudden jump. However, power output varies in a similar manner for all considered bluff bodies and angles of attack. More specifically, for lower flow velocities (e.g., $U = 4$ m/s), two optimal values of load resistances exist (i.e., the two peaks of the power outputs as shown in the figures). On the other hand, for higher flow velocities (e.g., $U = 14$ m/s), the power output reaches the maximum value around $R = 10^5$ Ω. In the ranges of load resistances with lower displacements, larger power outputs are achieved. These observations have been discussed in detail in [45]. For $U = 4$ and 8 m/s, the maximum power output is exhibited by the $b/d = 2.0$ cylinder at a 0° angle of attack and a load resistance around $R = 10^5$ Ω. On the other hand, for $U = 14$ m/s, the maximum power output is exhibited by the $b/d = 1.0$ cylinder at the same angle of attack and load resistance.

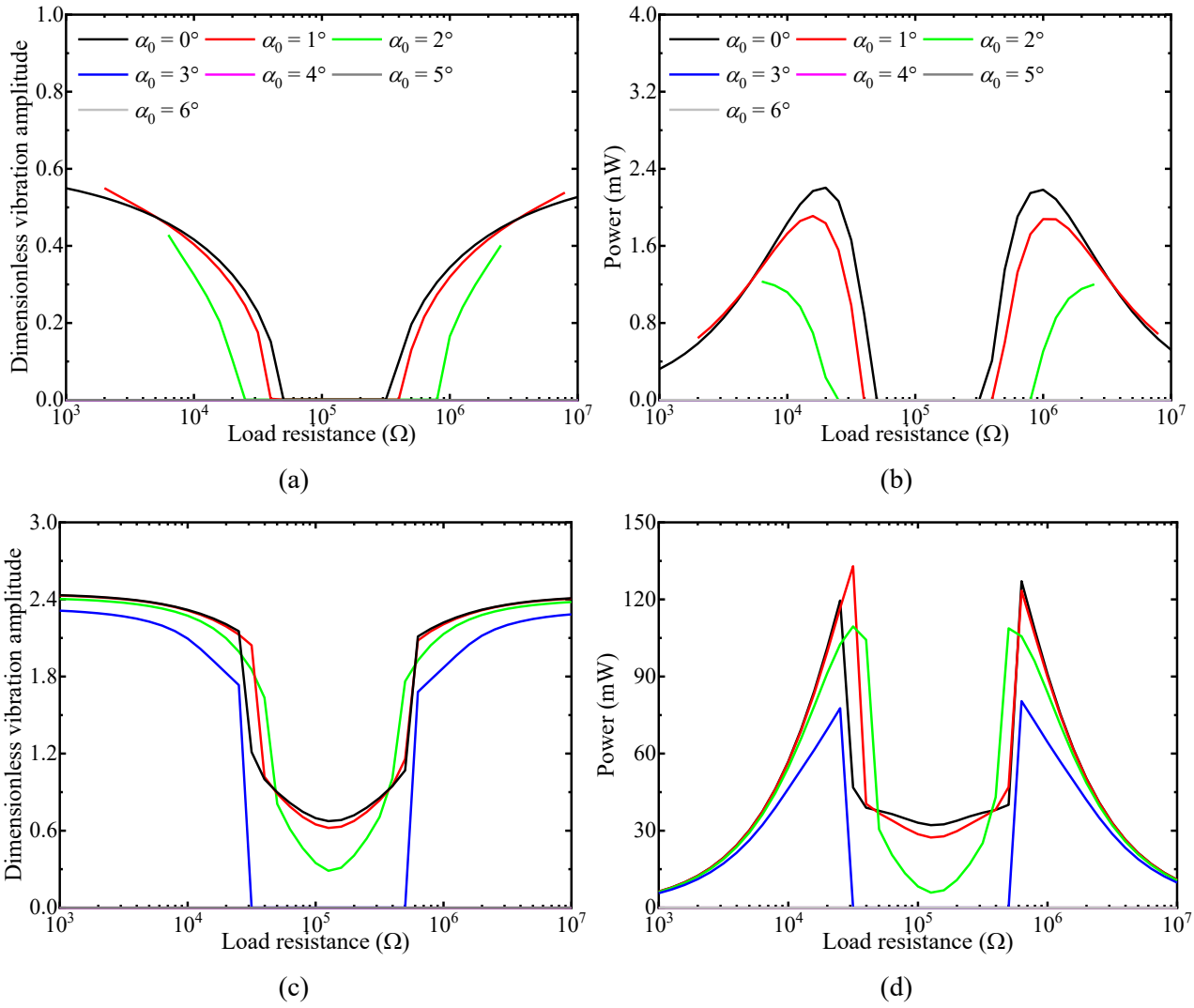

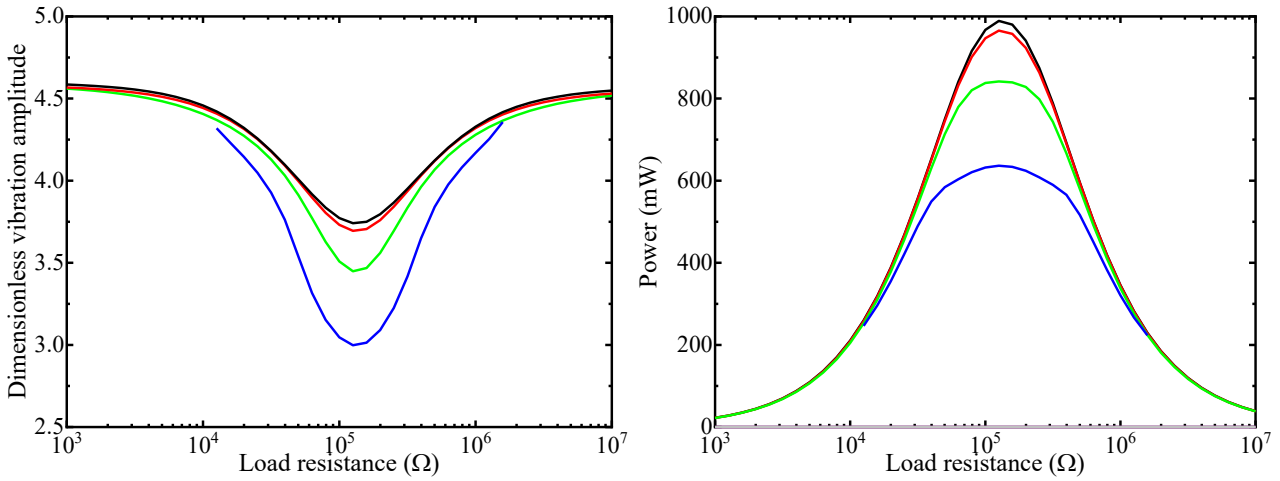


(e) (f)

**Figure 5.** Variation of transverse displacement and power output versus electrical load resistance for energy harvesters with rectangular cylinder of $b/d = 1.0$: (a) and (b) $U = 4$ m/s, (c) and (d) $U = 8$ m/s, (e) and (f) $U = 14$ m/s.

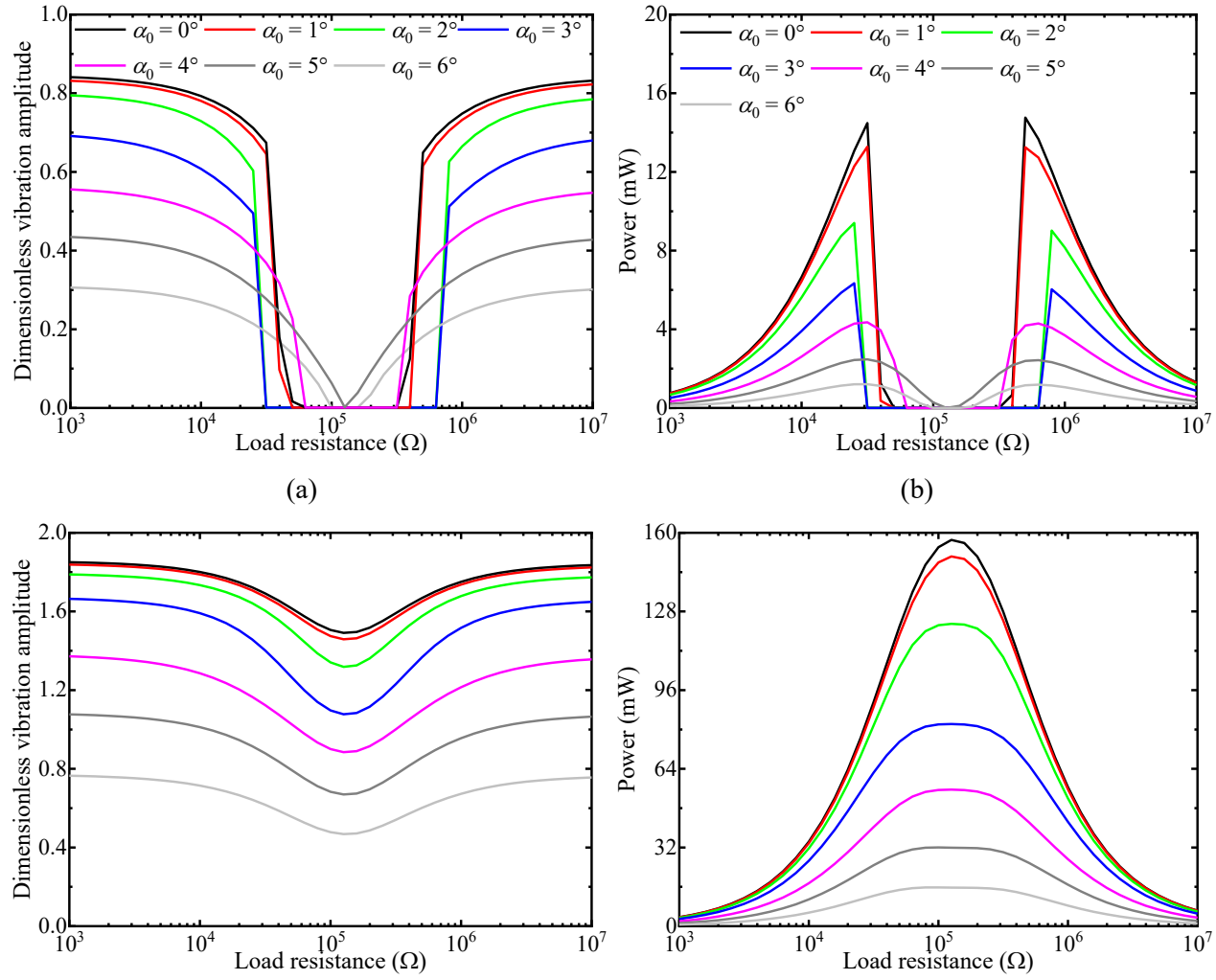


(a) (b)




(c) (d)

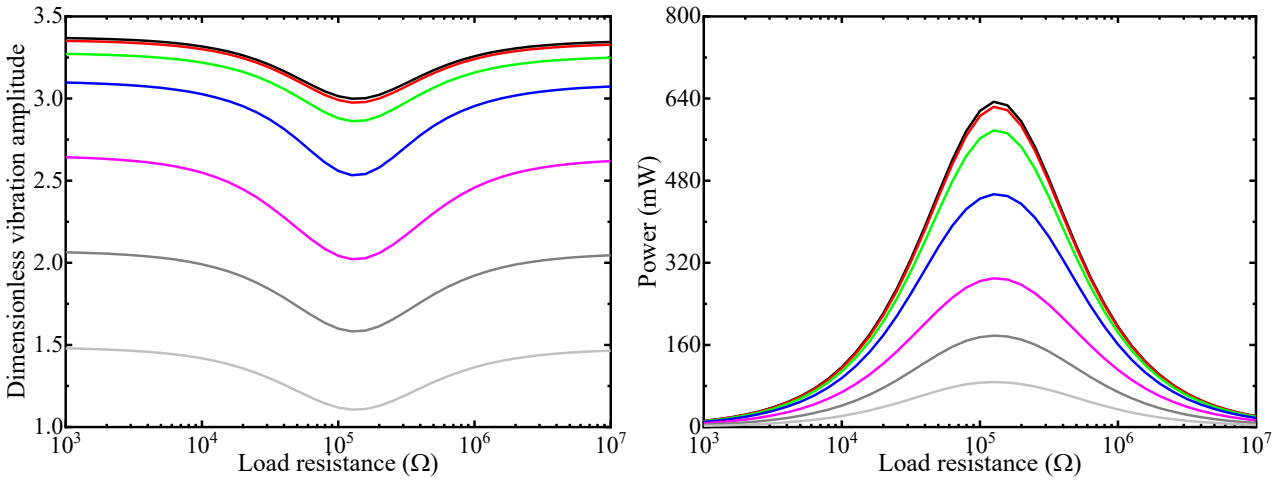


(e) (f)

**Figure 6.** Variation of transverse displacement and power output versus electrical load resistance for energy harvesters with rectangular cylinder of $b/d = 1.62$: (a) and (b) $U = 4$ m/s, (c) and (d) $U = 8$ m/s, (e) and (f) $U = 14$ m/s.

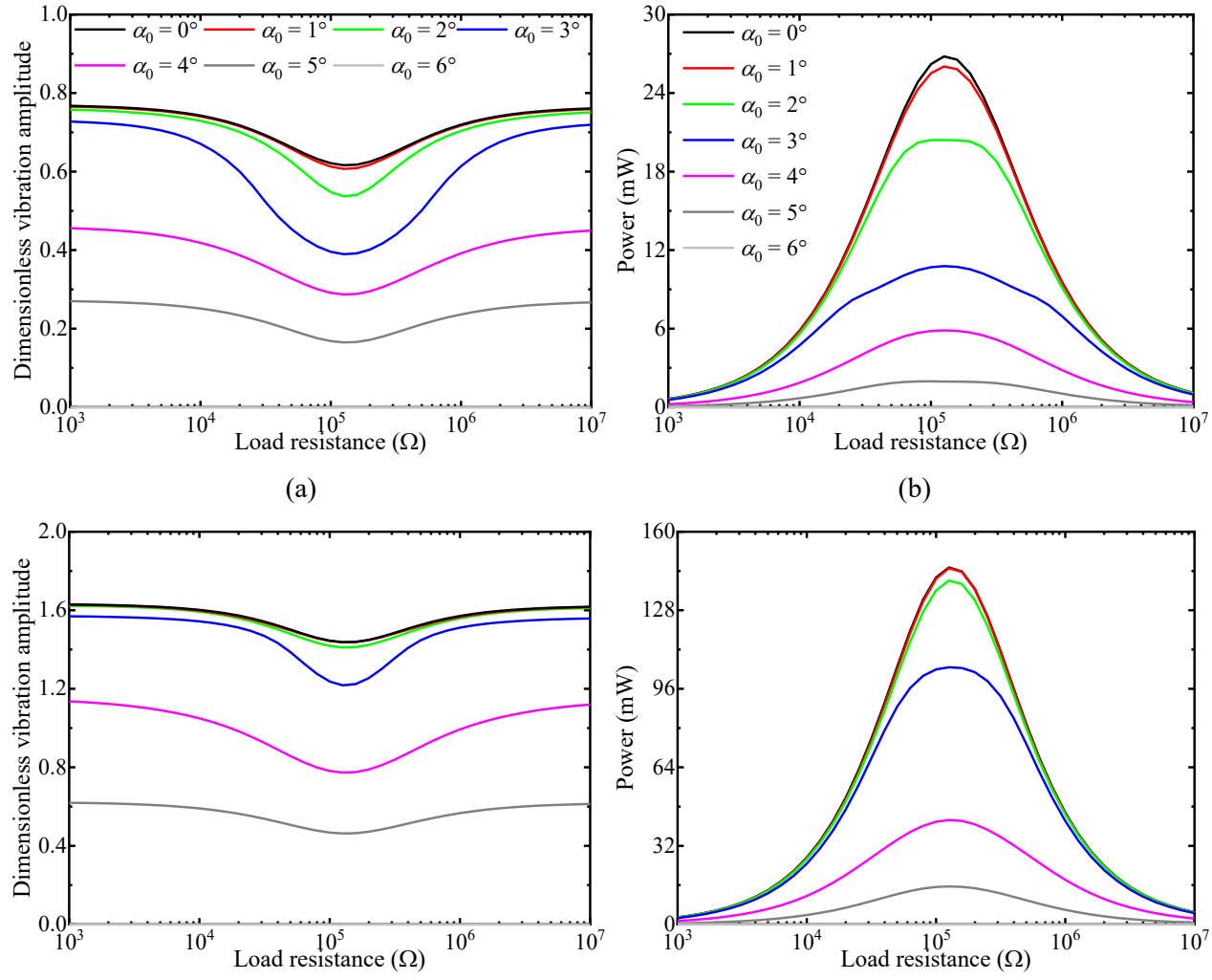


(a) (b)




(c) (d)

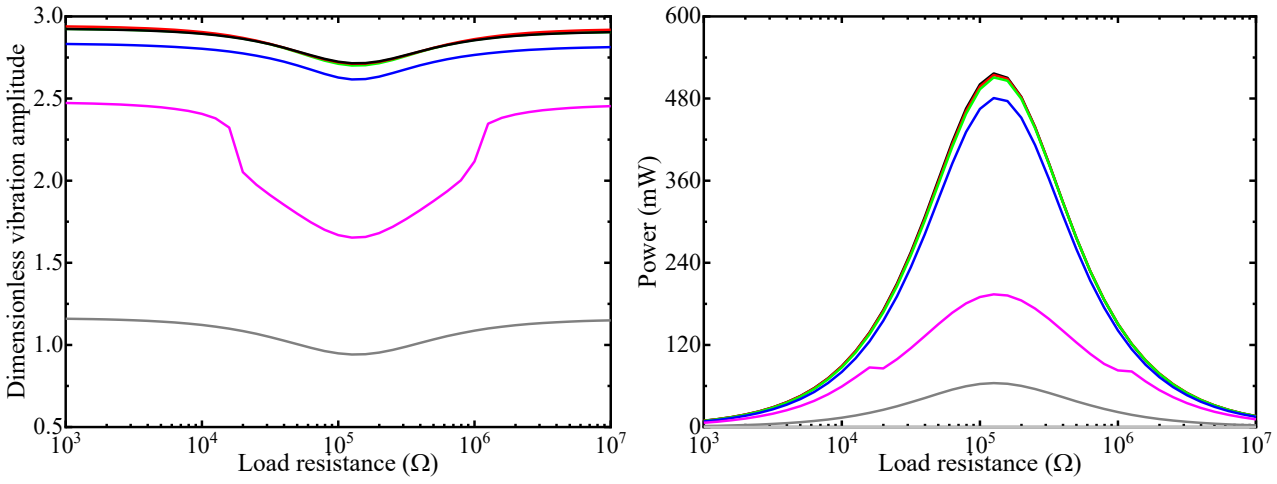


(e) (f)

**Figure 7.** Variation of transverse displacement and power output versus electrical load resistance for energy harvesters with rectangular cylinder of $b/d = 2.0$: (a) and (b) $U = 4$ m/s, (c) and (d) $U = 8$ m/s, (e) and (f) $U = 14$ m/s.

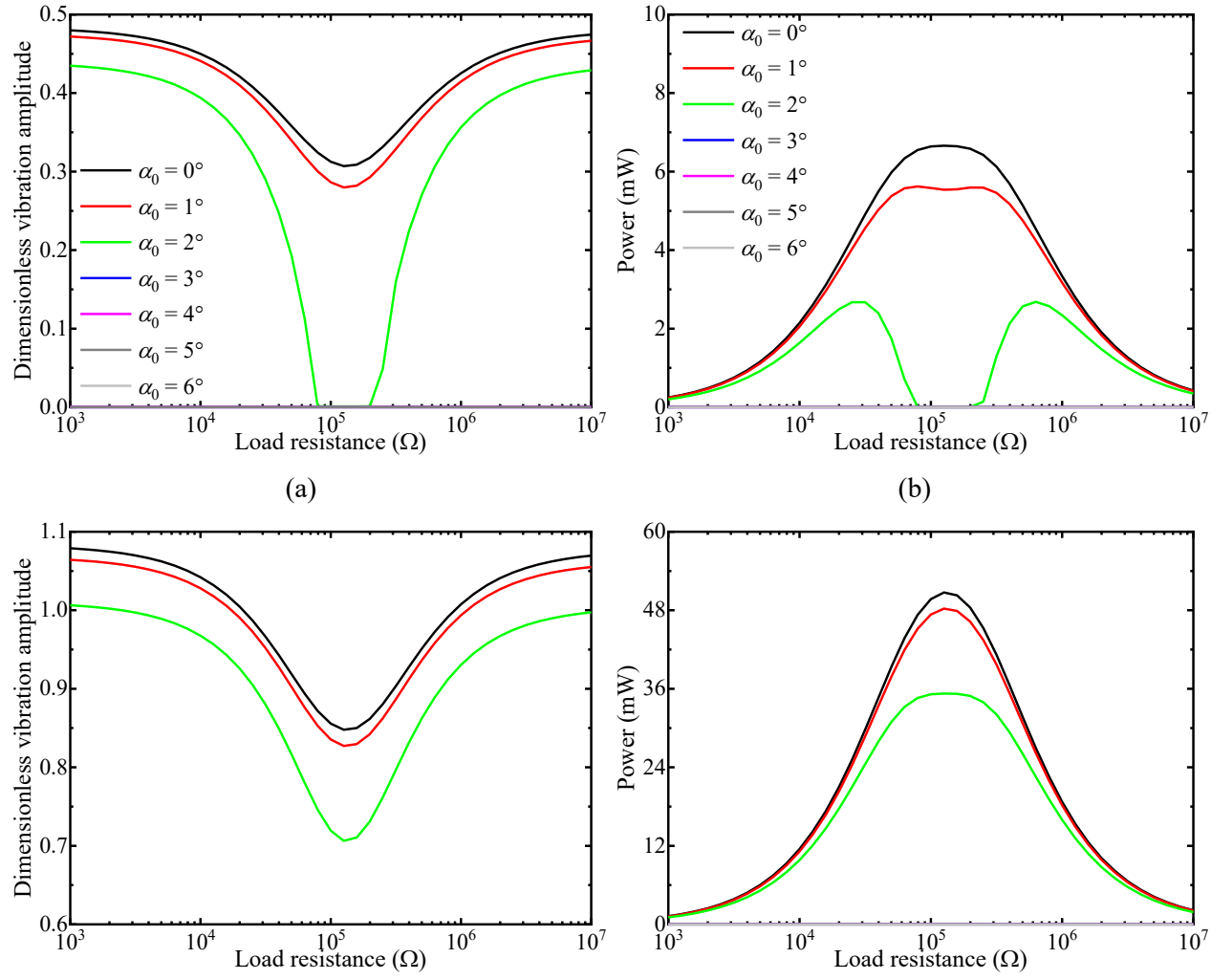


(a) (b)




(c) (d)

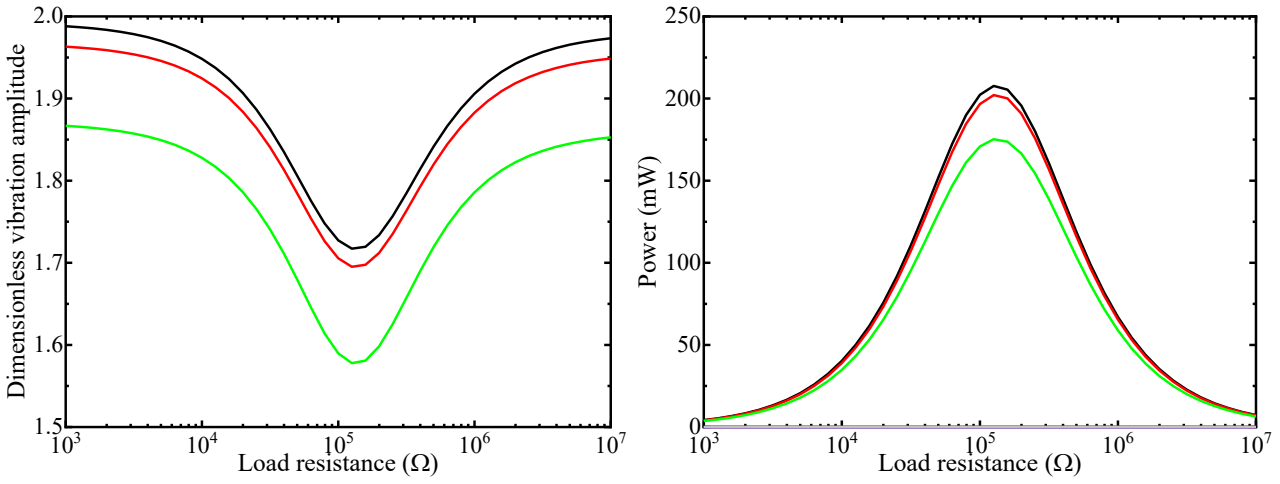


(e) (f)

**Figure 8.** Variation of transverse displacement and power output versus electrical load resistance for energy harvesters with rectangular cylinder of $b/d = 2.50$: (a) and (b) $U = 4$ m/s, (c) and (d) $U = 8$ m/s, (e) and (f) $U = 14$ m/s.

Figures 9 ~ 12 present the effects of the angle of attack on the transverse displacements of the energy harvesters and power outputs for energy harvesters with different bluff bodies. The results are given for two load resistances, i.e., $R = 10^5$ and $10^6$ Ω, respectively. It is noted that both the onset velocities and the slopes of the bifurcation curves are affected by the angle of attack. All rectangular cylinders exhibit the largest transverse displacements and power outputs at the angle of attack $\alpha_0 = 0°$, while the values at $\alpha_0 = 1°$ and 2° are only slightly lower than those at $\alpha_0 = 0°$. For the $b/d = 1.0$ cylinder, no galloping vibration occurs $\alpha_0 = 4°$, 5°, and 6°; for the $b/d = 2.0$ section, no galloping vibration occurs at $\alpha_0 = 6°$; for the $b/d = 2.5$ section, no galloping vibration occurs at $\alpha_0 = 3°$, 4°, 5°, and 6°. These are expected from the linear analysis either because the cylinder is stable from galloping at the associated angle of attack or because the onset galloping velocity is higher than 15 m/s. For the $b/d = 1.0$ and 2.0 cylinders, although the onset velocities are insignificantly affected by the angle of attack, the cylinders exhibit very different galloping responses at various angles of attack. It is also interesting to note that the transverse displacements are much lower while the power outputs are much higher at the load resistance values of $R = 10^5$ Ω, which is consistent with the observations in Figures 5 ~ 9.

A comparison of Figures 9 ~ 12 suggests that, within the considered range of wind velocities, the largest vibration amplitude and the largest power output are achieved by the $b/d = 1.0$ cylinder at a 0° angle of attack and a flow velocity of 15 m/s. Unfortunately, the performance of the energy harvester with the $b/d = 1.0$ cylinder is rather sensitive to the angle of attack, resulting in a zero power output as the angle of attack is increased over 4°. On the other hand, the energy harvester with the $b/d = 1.62$ cylinder produces lower power output than that produced by the $b/d = 1.0$ cylinder at a 0° angle of attack. However, the $b/d = 1.62$ cylinder is

always effective within the analyzed range of angles of attack, although the power output reduces with increasing the angle of attack. The $b/d$ = 2.0 cylinder is also effective within a relatively wide range of angles of attack, while its power output is lower than that of the $b/d$ = 1.62 cylinder. The power output of the $b/d$ = 2.5 cylinder is the lowest among the analyzed cylinders, and its performance is also quite sensitive to the angle of attack. In conclusion, the $b/d$ = 1.0 rectangular cylinder is suggested if the energy harvester is expected to produce large power output in a well-controlled flow with a 0° angle of attack. On the other hand, the $b/d$ = 1.62 rectangular cylinder should be recommended if the energy harvester is expected to be effective within a relatively wide range of angles of attack.

Inspecting the plotted bifurcation diagrams in Figures 9 ~ 12, it is clear that the predefined angle of attack may change the bifurcation behavior of the energy harvester. As an example, for the $b/d$ = 1.62 cylinder shown in Figure 10, when the predefined angle of attack is 0° ~ 4°, a saddle-node bifurcation with the presence of a subcritical jump takes place. The saddle-node and subcritical Hopf bifurcations disappear while a supercritical Hopf bifurcation occurs at the onset galloping velocity when the predefined angle of attack is increased to higher values ($\alpha_0$ = 5° and 6°). To better interpret these bifurcations, the transverse displacements and power outputs for energy harvesters with the $b/d$ = 1.62 rectangular cylinder at $\alpha_0$ = 3° and 6° are calculated from different initial amplitudes. By varying the initial amplitude, both unstable and stable limit cycles can be captured. The amplitude of an unstable limit cycle lies between two successive initial amplitudes which produce different steady-state responses. The steady-state displacements and power outputs are presented in Figure 13, in which solid lines represent the steady-state amplitudes of stable limit cycles, while dashed lines represent those of unstable limit cycles. The steady-state displacements and power outputs calculated by increasing the flow velocity are also given in Figure 13. Some displacement time-histories from different initial displacements are given in Figure 14, in which $Y(0)$ is the initial displacement. As shown in Figure 13, the saddle-node and subcritical Hopf bifurcations can be clearly observed for the $b/d$ = 1.62 rectangular cylinder at $\alpha_0$ = 3°. The steady-state displacements and power outputs are dependent on the initial displacement for flow velocities between the saddle-node and subcritical Hopf bifurcations, as verified in Figure 14(a) by the displacement time-histories at $U$ = 6 m/s. The increasing velocity curves in Figure 13 cannot capture the stable and unstable limit cycles between the saddle-node and subcritical Hopf bifurcations. The steady-state displacements and power outputs become independent of the initial displacement after the subcritical Hopf bifurcation, as illustrated in Figure 14(b) by the displacement time-histories at $U$ = 8 m/s. The $b/d$ = 1.62 rectangular cylinder at $\alpha_0$ = 3°exhibits a supercritical Hopf bifurcation at the onset galloping velocity. The steady-state displacements and power outputs are always independent of the initial displacement, as illustrated

in Figure 14(c) by the displacement time-histories at $U = 5$ m/s. The increasing velocity curves are consistent with the curves calculated with different initial displacements, and hence the later ones are covered by the former ones.

The preceding discussions mean that the predefined angle of attack and bluff body configuration may strongly affect the onset velocity of galloping as well as the type of instability of the system. For a case that exhibits a single supercritical Hopf bifurcation at the onset galloping velocity, the vibration amplitude increases continuously with increasing the flow velocity. Hence, the vibration amplitude and the power output for such a case also vary continuously with the load resistance, as demonstrated by the $b/d = 1.62$ cylinder at $\alpha_0 = 5°$ shown in Figure 6. On the other hand, for a case that exhibits the saddle-node bifurcation, the vibration amplitude has a sharp jump with increasing the flow velocity, which occurs as a result of the hysteresis behavior in the changing of the displacement amplitude versus flow velocity, as demonstrated by the $b/d = 1.0$ cylinder at $\alpha_0 = 0°$ shown in Figure 9. If the simulations were performed by decreasing the oncoming flow velocity, the jump of the vibration amplitude would occur at a lower flow velocity. At lower flow velocities, the vibration may belong to the branches before or after the sharp jump depending on the load resistance. Hence, there are sharp jumps in the variations of the vibration amplitude and the power output versus the load resistance, as demonstrated by the $b/d = 1.0$ cylinder at $\alpha_0 = 0°$ shown in Figures 5(a, b, c, d). At higher flow velocities, the vibrations always belong to the branch after the sharp jump, and hence the vibration amplitude varies continuously with the load resistance, as shown in Figures 5(e, f).

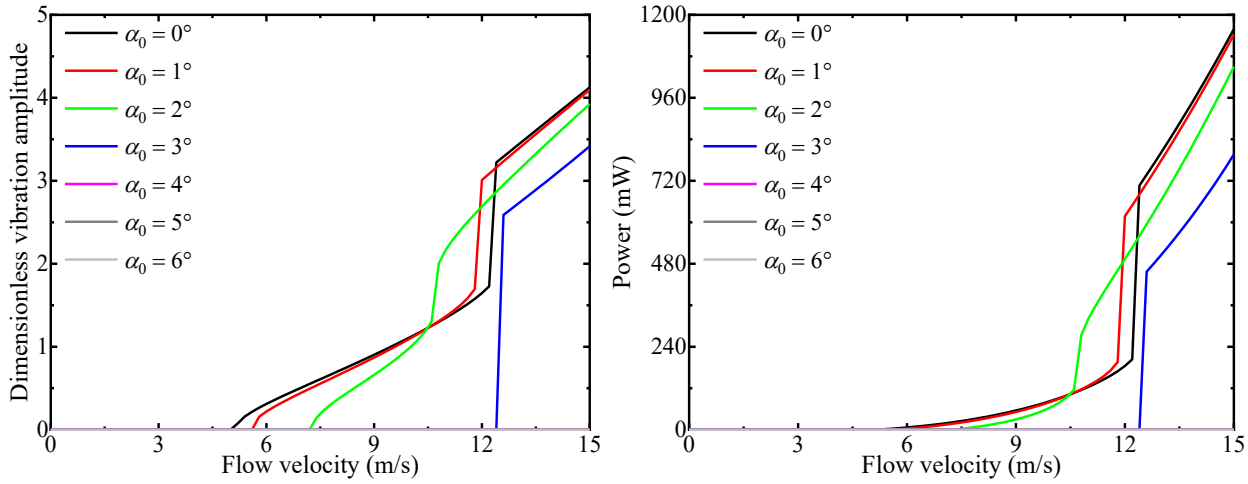


(a) (b)

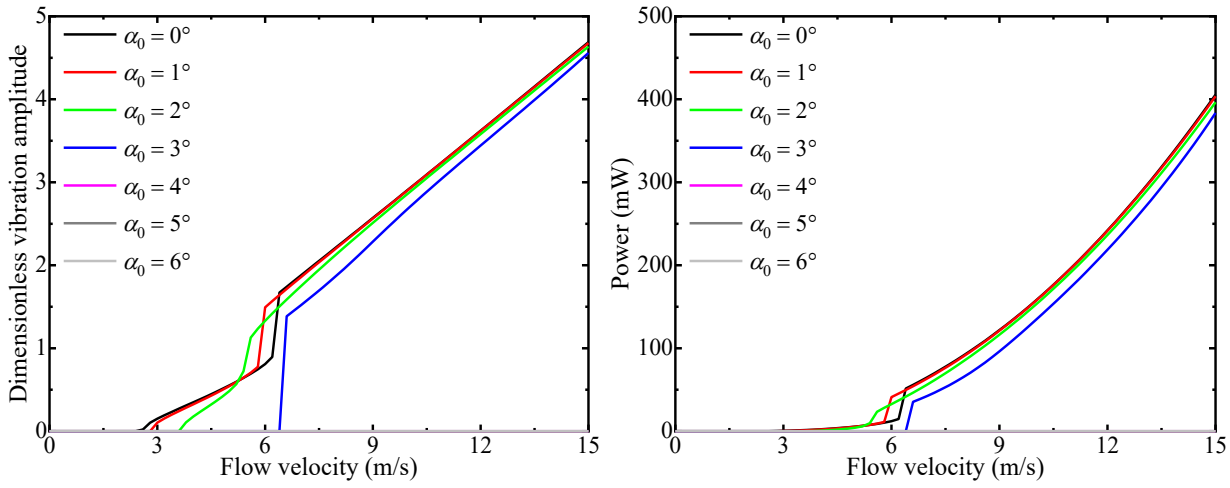


**Figure 9.** Bifurcation diagrams for transverse displacements and power outputs of energy harvesters with rectangular cylinder of $b/d = 1.0$: (a) and (b) $R = 10^5$ Ω; (c) and (d) $R = 10^6$ Ω.

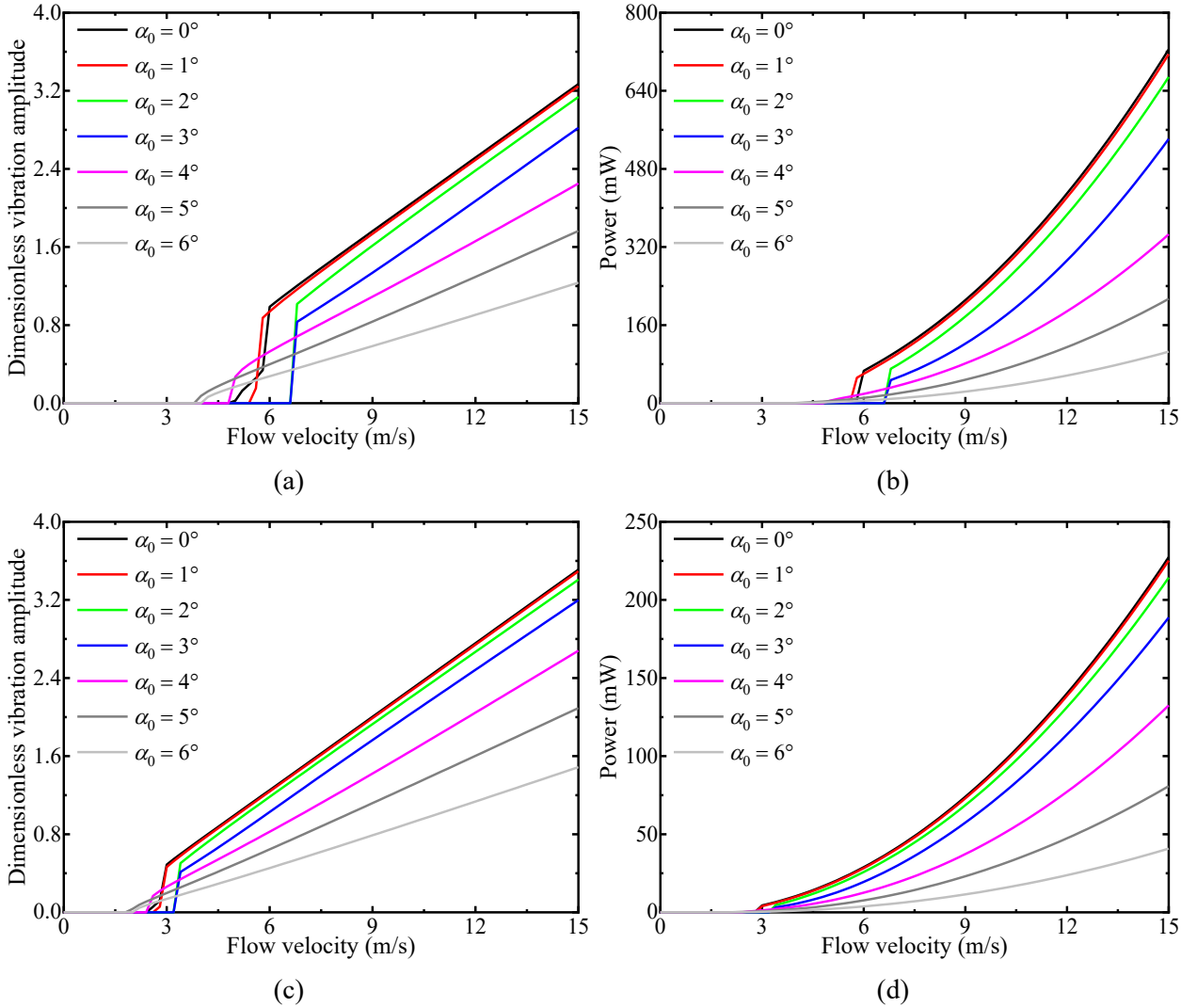


**Figure 10.** Bifurcation diagrams for transverse displacements and power outputs of energy harvesters with rectangular cylinder of $b/d = 1.62$: (a) and (b) $R = 10^5$ Ω; (c) and (d) $R = 10^6$ Ω.

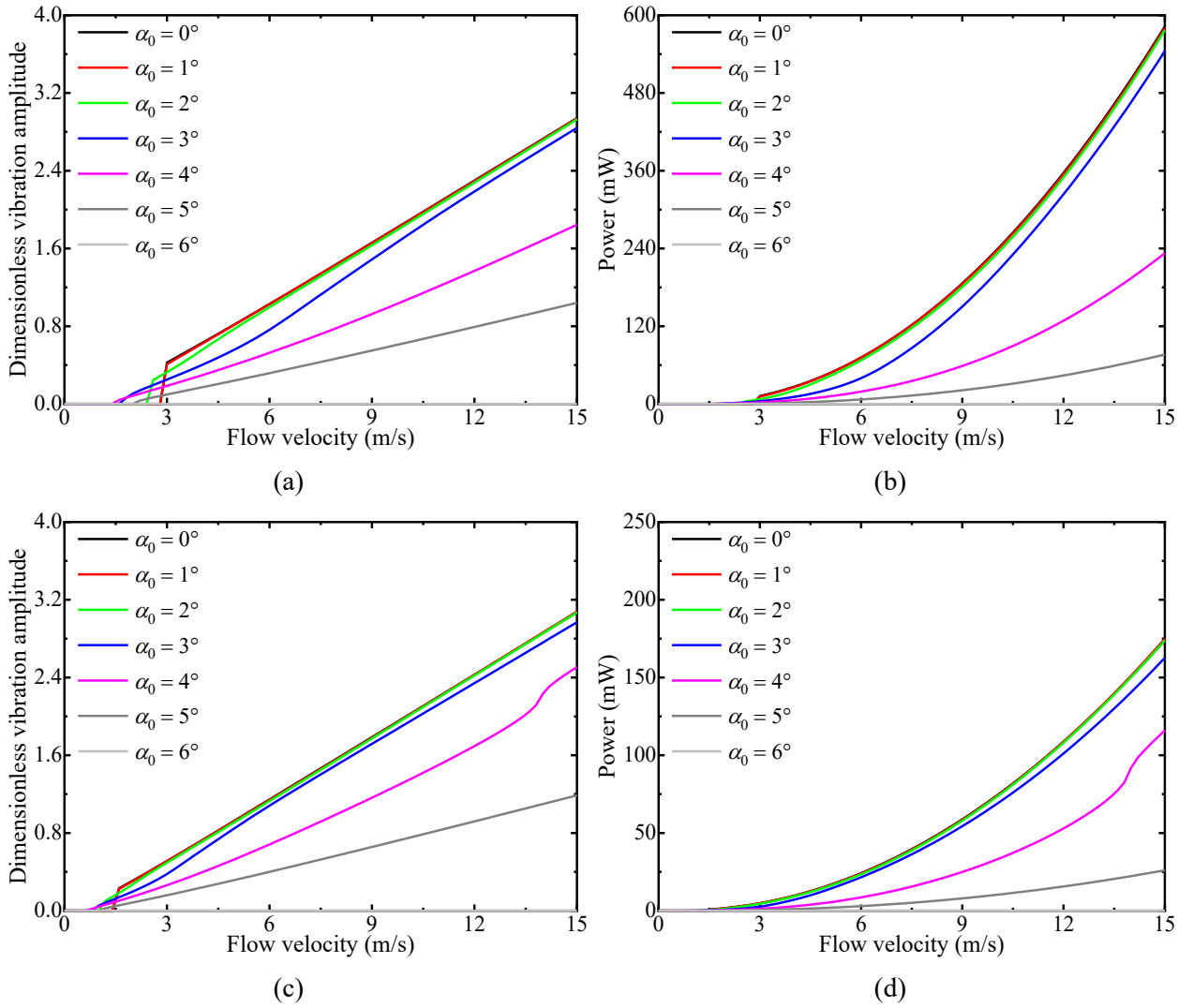


**Figure 11.** Bifurcation diagrams for transverse displacements and power outputs of energy harvesters with rectangular cylinder of $b/d$ = 2.0: (a) and (b) $R = 10^5$ Ω; (c) and (d) $R = 10^6$ Ω.

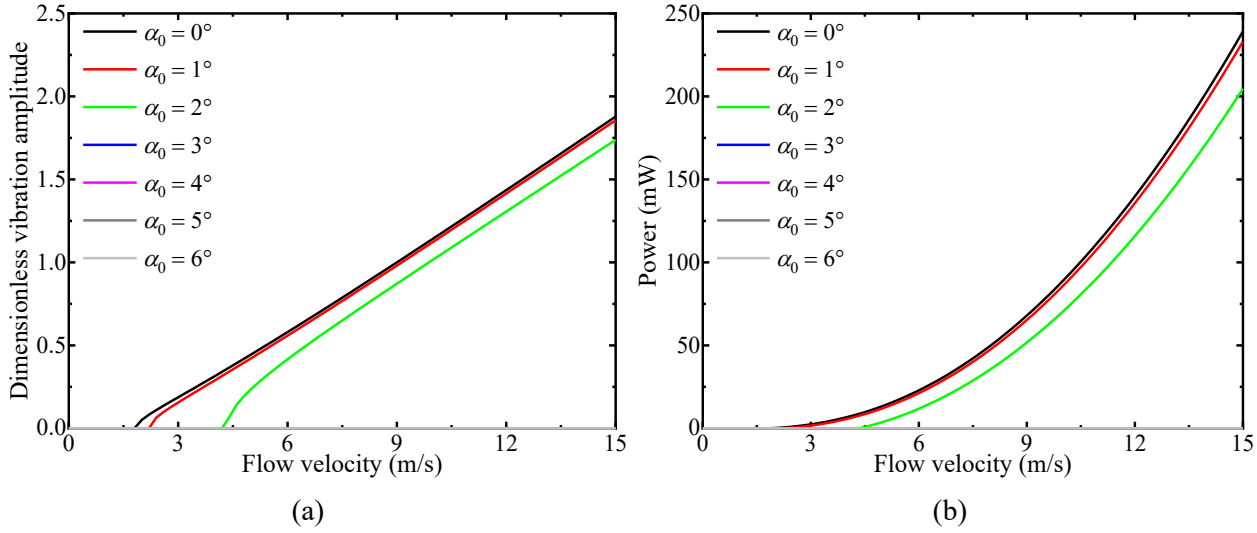

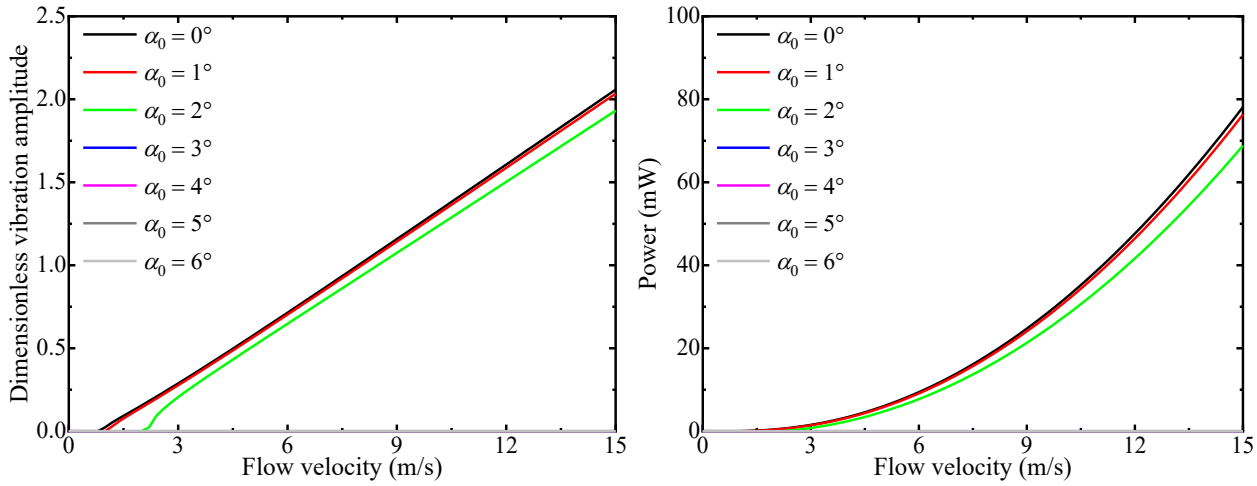


(c) (d)

**Figure 12.** Bifurcation diagrams for transverse displacements and power outputs of energy harvesters with rectangular cylinder of $b/d = 2.50$: (a) and (b) $R = 10^5$ Ω; (c) and (d) $R = 10^6$ Ω.

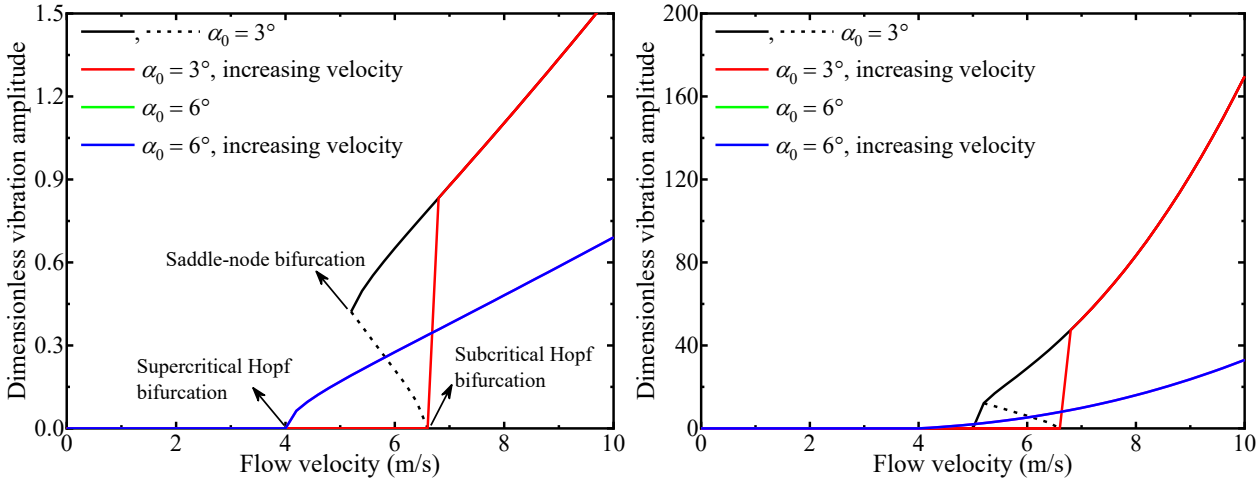


(a) (b)

**Figure 13.** Transverse displacements (a) and power outputs (a) of energy harvesters with rectangular cylinder of $b/d = 1.62$ at $\alpha_0 = 3°$ and 6°

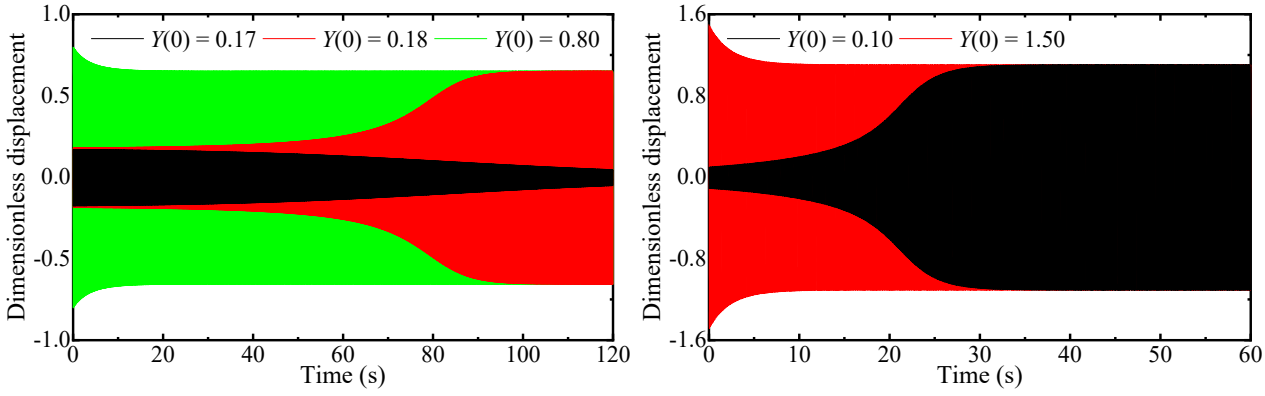


(a) (b)

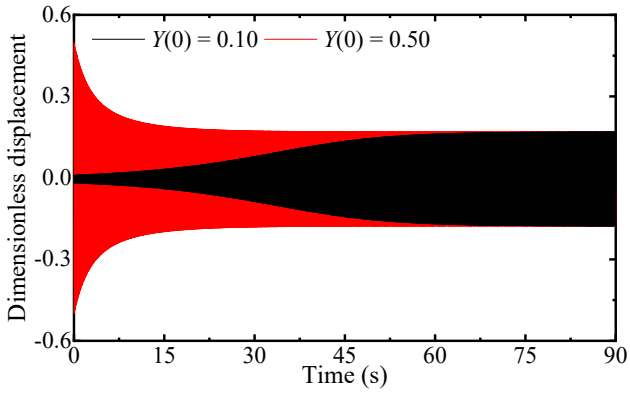


(c)

**Figure 14.** Transverse displacement time-histories of energy harvesters with rectangular cylinder of $b/d$ = 1.62: (a) $\alpha_0$ = 3° and $U$ = 6 m/s, (b) $\alpha_0$ = 3° and $U$ = 8 m/s, and (c) $\alpha_0$ = 6° and $U$ = 5 m/s.

## 4. Conclusions

This paper presented a numerical investigation to study the influences of the predefined angle of attack on transverse galloping-based energy harvesting using different cross-sections as the tip body. The galloping-based energy harvester is considered as a lumped-parameter model with linear mechanical and electrical parameters, while the nonlinear aerodynamic forces are simulated using the quasi-steady model. Bluff bodies with six different cross-sections were considered: rectangular sections of the side ratio $b/d$ = 1.0, 1.62, 2.0, and 2.5, the trapezium section, and the angle section.

Numerical results show that the onset velocities for the $b/d$ = 1.0 and 2.5 rectangular cylinders increase significantly with increasing the angle of attack. For the other bluff bodies, the onset velocities vary non-monotonically with increasing the angle of attack, and the effects of the angle of attack on the onset velocities are less significant. At the angle of attack $\alpha_0$ = 0°, the onset galloping velocities of the rectangular cylinders can be decreased by increasing the side ratio, and the lowest onset velocity is achieved by the $b/d$ = 2.5 rectangular cylinder. On the other hand, the $b/d$ = 1.62 and 2.0 rectangular cylinders should be recommended if the energy harvester is expected to have low onset velocities within a relatively wide range of angle of attack. The trapezium section and the angle section are not suitable for energy harvesting due to their very high onset velocities within the considered range of angles of attack.

The largest vibration amplitude and the largest power output are achieved by the $b/d$ = 1.0 cylinder at a 0° angle of attack. Therefore, the $b/d$ = 1.0 rectangular cylinder is suggested if the energy harvester is expected to produce large power outputs in a well-controlled flow with an angle of attack around 0°. Unfortunately, the performance of the energy harvester with the $b/d$ = 1.0 cylinder is rather sensitive to the angle of attack, resulting in a zero power output as the angle of attack is increased over 4°. The energy harvester with the $b/d$ = 1.62 cylinder produces lower power output than that produced by the $b/d$ = 1.0 cylinder at a 0° angle of

attack. However, the $b/d$ = 1.62 cylinder is always effective within the analyzed range of angles of attack, and hence this cylinder should be recommended if the energy harvester is expected to be effective within a relatively wide range of angles of attack. The $b/d$ = 2.0 cylinder is also effective within a relatively wide range of angles of attack, while its power output is lower than that of the $b/d$ = 1.62 cylinder. The power output of the $b/d$ = 2.5 cylinder is the lowest among the analyzed cylinders, and its performance is also quite sensitive to the angle of attack.

**Credit author statement**

**Mingjie Zhang:** Conceptualization, methodology, data analysis, writing original draft. **Haiyan Yu:** Data analysis, writing original draft. **Daniil Yurchenko:** Conceptualization, writing original draft. **Junlei Wang:** Conceptualization, validation, methodology. **Fuyou Xu:** Conceptualization, validation, methodology. **Cristoforo Demartino:** Methodology, writing original draft.

**Declaration of competing interest**

The authors declare that they have no known competing financial interests or personal relationships that could have appeared to influence the work reported in this paper.

**References**

[1] Zhang M, Xu F, Zhang Z, Ying X. Energy budget analysis and engineering modeling of post-flutter limit cycle oscillation of a bridge deck. Journal of Wind Engineering and Industrial Aerodynamics. 2019;188:410-20.

[2] Parkinson G, Smith J. The square prism as an aeroelastic non-linear oscillator. The Quarterly Journal of Mechanics and Applied Mathematics. 1964;17(2):225-39.

[3] Zhang M, Xu F, Han Y. Assessment of wind-induced nonlinear post-critical performance of bridge decks. Journal of Wind Engineering and Industrial Aerodynamics. 2020;203:104251.

[4] Zhao J, Hourigan K, Thompson M. Flow-induced vibration of D-section cylinders: An afterbody is not essential for vortex-induced vibration. Journal of Fluid Mechanics. 2018;851:317-43.

[5] Seyed-Aghazadeh B, Carlson DW, Modarres-Sadeghi Y. Vortex-induced vibration and galloping of prisms with triangular cross-sections. Journal of Fluid Mechanics. 2017;817:590.

[6] Xu F, Yu H, Zhang M, Han Y. Experimental study on aerodynamic characteristics of a large-diameter ice-accreted cylinder without icicles. Journal of Wind Engineering and Industrial Aerodynamics.208:104453.

[7] Novak M. Galloping oscillations of prismatic structures. Journal of Engineering Mechanics. 1972.

[8] Parkinson G, Wawzonek M. Some considerations of combined effects of galloping and vortex resonance. Journal of Wind Engineering and Industrial Aerodynamics. 1981;8(1-2):135-43.

[9] Abdelkefi A, Yan Z, Hajj MR. Performance analysis of galloping-based piezoaeroelastic energy harvesters with different cross-section geometries. Journal of Intelligent Material Systems and Structures. 2014;25(2):246-56.

[10] Barrero-Gil A, Sanz-Andrés A, Alonso G. Hysteresis in transverse galloping: the role of the inflection points. Journal of Fluids and Structures. 2009;25(6):1007-20.

[11] Qin W, Deng W, Pan J, Zhou Z, Du W, Zhu P. Harvesting wind energy with bi-stable snap-through excited by vortex-induced vibration and galloping. Energy. 2019;189:116237.

[12] Sun H, Ma C, Bernitsas MM. Hydrokinetic power conversion using Flow Induced Vibrations with cubic restoring force. Energy. 2018;153:490-508.

[13] Sun W, Jo S, Seok J. Development of the optimal bluff body for wind energy harvesting using the synergetic effect

of coupled vortex induced vibration and galloping phenomena. International Journal of Mechanical Sciences. 2019;156:435-45.
[14] Zhu H, Gao Y. Hydrokinetic energy harvesting from flow-induced vibration of a circular cylinder with two symmetrical fin-shaped strips. Energy. 2018;165:1259-81.
[15] Zhang B, Wang K-H, Song B, Mao Z, Tian W. Numerical investigation on the effect of the cross-sectional aspect ratio of a rectangular cylinder in FIM on hydrokinetic energy conversion. Energy. 2018;165:949-64.
[16] Den Hartog JP. Mechanical vibrations: Courier Corporation, 1985.
[17] Parkinson G, Brooks N. On the aeroelastic instability of bluff cylinders. 1961.
[18] Luo S, Chew Y, Ng Y. Hysteresis phenomenon in the galloping oscillation of a square cylinder. Journal of Fluids and Structures. 2003;18(1):103-18.
[19] Dai H, Abdelkefi A, Wang L. Usefulness of passive non-linear energy sinks in controlling galloping vibrations. International Journal of Non-Linear Mechanics. 2016;81:83-94.
[20] Abdel-Rohman M. Design of tuned mass dampers for suppression of galloping in tall prismatic structures. Journal of Sound and Vibration. 1994;171(3):289-99.
[21] Mannini C, Marra A, Bartoli G. VIV–galloping instability of rectangular cylinders: Review and new experiments. Journal of wind engineering and industrial aerodynamics. 2014;132:109-24.
[22] Tamura T, Miyagi T. The effect of turbulence on aerodynamic forces on a square cylinder with various corner shapes. Journal of Wind Engineering and Industrial Aerodynamics. 1999;83(1-3):135-45.
[23] Lou W, Huang C, Huang M, Yu J. An aerodynamic anti-galloping technique of iced 8-bundled conductors in ultra-high-voltage transmission lines. Journal of Wind Engineering and Industrial Aerodynamics. 2019;193:103972.
[24] Barrero-Gil A, Alonso G, Sanz-Andres A. Energy harvesting from transverse galloping. Journal of Sound and Vibration. 2010;329(14):2873-83.
[25] Vicente-Ludlam D, Barrero-Gil A, Velazquez A. Optimal electromagnetic energy extraction from transverse galloping. Journal of Fluids and Structures. 2014;51:281-91.
[26] Vicente-Ludlam D, Barrero-Gil A, Velazquez A. Enhanced mechanical energy extraction from transverse galloping using a dual mass system. Journal of Sound and Vibration. 2015;339:290-303.
[27] Abdelkefi A, Hajj M, Nayfeh A. Piezoelectric energy harvesting from transverse galloping of bluff bodies. Smart Materials and Structures. 2012;22(1):015014.
[28] Abdelkefi A, Hajj MR, Nayfeh AH. Power harvesting from transverse galloping of square cylinder. Nonlinear Dynamics. 2012;70(2):1355-63.
[29] Abdelkefi A, Yan Z, Hajj MR. Modeling and nonlinear analysis of piezoelectric energy harvesting from transverse galloping. Smart materials and Structures. 2013;22(2):025016.
[30] Javed U, Abdelkefi A. Impacts of the aerodynamic force representation on the stability and performance of a galloping-based energy harvester. Journal of Sound and Vibration. 2017;400:213-26.
[31] Javed U, Abdelkefi A. Role of the galloping force and moment of inertia of inclined square cylinders on the performance of hybrid galloping energy harvesters. Applied Energy. 2018;231:259-76.
[32] Yang Y, Zhao L, Tang L. Comparative study of tip cross-sections for efficient galloping energy harvesting. Applied Physics Letters. 2013;102(6):064105.
[33] Zhao L, Tang L, Yang Y. Comparison of modeling methods and parametric study for a piezoelectric wind energy harvester. Smart materials and Structures. 2013;22(12):125003.
[34] Hémon P, Amandolese X, Andrianne T. Energy harvesting from galloping of prisms: A wind tunnel experiment. Journal of Fluids and Structures. 2017;70:390-402.
[35] Andrianne T, Aryoputro RP, Laurent P, Colson G, Amandolese X, Hémon P. Energy harvesting from different aeroelastic instabilities of a square cylinder. Journal of Wind Engineering and Industrial Aerodynamics. 2018;172:164-9.
[36] Zhang B, Mao Z, Song B, Ding W, Tian W. Numerical investigation on effect of damping-ratio and mass-ratio on energy harnessing of a square cylinder in FIM. Energy. 2018;144:218-31.

[37] Nemes A, Zhao J, Jacono DL, Sheridan J. The interaction between flow-induced vibration mechanisms of a square cylinder with varying angles of attack. 2012.
[38] Zhao J, Leontini JS, Jacono DL, Sheridan J. Fluid–structure interaction of a square cylinder at different angles of attack. Journal of Fluid Mechanics. 2014;747:688-721.
[39] Zhang M, Abdelkefi A, Yu H, Ying X, Gaidai O, Wang J. Predefined angle of attack and corner shape effects on the effectiveness of square-shaped galloping energy harvesters. Applied Energy. 2021;302:117522.
[40] Wang J, Gu S, Abdelkefi A, Zhang M, Xu W, Lai Y. Piezoelectric energy harvesting from flow-induced vibrations of a square cylinder at various angles of attack. Smart Materials and Structures. 2021.
[41] Norberg C. Flow around rectangular cylinders: pressure forces and wake frequencies. Journal of wind engineering and industrial aerodynamics. 1993;49(1-3):187-96.
[42] Feero MA, Naguib AM, Koochesfahani MM. Influence of geometry on the galloping instability of rectangular cylinders in the Reynolds number range 1,000–10,000. Journal of Fluids and Structures. 2020;94:102881.
[43] Luo S, Yazdani MG, Chew Y, Lee T. Effects of incidence and afterbody shape on flow past bluff cylinders. Journal of wind engineering and industrial aerodynamics. 1994;53(3):375-99.
[44] Slater JE. Aeroelastic instability of a structural angle section: University of British Columbia, 1969.
[45] Yu H, Zhang M. Effects of side ratio on energy harvesting from transverse galloping of a rectangular cylinder. Energy. 2021;226:120420.
[46] Ma C, Liu Y, Li Q, Liao H. Prediction and explanation of the aeroelastic behavior of a square-section cylinder via forced vibration. Journal of Wind Engineering and Industrial Aerodynamics. 2018;176:78-86.
[47] Washizu K, Ohya A, Otsuki Y, Fujii K. Aeroelastic instability of rectangular cylinders in a heaving mode. Journal of Sound and Vibration. 1978;59(2):195-210.
[48] Strogatz SH. Nonlinear dynamics and chaos with student solutions manual: With applications to physics, biology, chemistry, and engineering: CRC press, 2018.